Effect of Silver Powder Microstructure on the Performance of Silver Powder and Front-Side Solar Silver Paste

Xianglei Yu , Hu Sun , Zuo Qian , Weichao Li , Wei Li , Fuchun Huang , Junpeng Li * , Guoyou Gan *

Posted Date: 27 December 2023

doi: 10.20944/preprints202312.1871.v1

Keywords: Silver powder; solar cell; aggregation growth; crystalline growth; sintering activity.

Article

Effect of Silver Powder Microstructure on the Performance of Silver Powder and Front-Side Solar Silver Paste

Xianglei Yu [1], Hu Sun [1], Zuo Qian [1], Weichao Li [2], Wei Li [3], Fuchuan Huang [3], Junpeng Li [3,*] and Guoyou Gan [1,*]

[1] Faculty of Material Science and Engineering, Kunming University of Science and Technology, Kunming 650093, China;
[2] R&D Center of Yunnan Tin Group (Holding) Co., Ltd, Kunming 650093, China;
[3] Sino-Platinum Metals Co., LTD, Kunming 650093, China;
* Correspondence: Guoyou Gan: ganguoyou@kust.edu.cn, Junpeng Li: lijunpeng@ipm.com.cn

Abstract: Silver powder, as the primary component of solar silver paste, significantly influences various aspects of paste performance, including printing, sintering, and conductivity. Silver powders prepared using the liquid-phase reduction method exhibit different microstructures depending on whether the growth process is dominated by aggregation or crystalline growth. This study explores the impact of different silver powder microstructures on packing density and sintering activity. It is observed that polycrystalline aggregated silver powder possesses higher surface energy, lower packing density, and greater sintering activity. Investigation into the influence of different silver powders on the electrical conductivity, adhesion, and structural density of silver paste reveals that polycrystalline aggregated silver powder is more suitable for lower sintering temperature pastes, whereas crystalline growth-type silver powder is better suited for higher sintering temperature pastes, resulting in a denser sintered silver layer. Finally, an analysis of the impact of various silver powders on the aspect ratio and electrical performance of solar cell silver grid lines yields higher aspect ratios (0.40) and photoelectric conversion efficiency (19.26%).

Keywords: silver powder; solar cell; aggregation growth; crystalline growth; sintering activity

1. Introduction

Photovoltaic power generation, as a method to harness abundant, clean, and reliable renewable energy, has seen rapid development against the backdrop of increasing global energy demand[1]. In 2022, the global photovoltaic installed capacity reached 230 GW, marking a substantial year-on-year growth of 35.3%. Within this landscape, crystalline silicon solar cells hold a dominant share, exceeding 90%, owing to their advantages such as low cost per unit of electricity, mature production processes, and extended lifespan[2,3]. The silver paste, especially the front-side silver paste, plays a pivotal role as a key material for fabricating electrodes in crystalline silicon solar cells. Its performance directly influences various aspects of solar cells, including series resistance (R_s), short-circuit current (I_{sc}), fill factor (FF), and photoelectric conversion efficiency (Eta)[4–6]. Typically, front-side silver paste comprises organic carriers, glass powder, and silver powder. The organic carrier primarily modulates the rheological properties of the silver paste to meet the dimensional and integrity requirements of fine grid lines for screen printing[7–9]. The glass powder serves to etch the SiNx antireflection layer and establish a favorable interface contact with the cell emitter[10–14]. Silver powder, constituting over 85% of the mass of solar silver paste, is the conductive phase and major component. The morphology, size, and sintering performance of silver powder directly impact the particle stacking before sintering, the formation and densification of the silver electrode conductive path during sintering, and the post-sintering properties of the electrode grid lines, including

 doi:10.20944/preprints202312.1871.v1

appearance, internal structure, resistivity, and contact resistance[15,16]. These aspects make silver powder a crucial factor in the study of the sintering process of solar silver paste.

The emitter of a solar cell employs high concentrations of ion doping to enhance photoelectric conversion efficiency. To mitigate the impact of high-temperature sintering on solar cell performance, the metallization sintering process for solar silver paste necessitates the use of as low a sintering temperature and as short a sintering time as possible. Typically, a belt furnace is employed for sintering, with the peak temperature ranging between 750-850 °C, which is below the melting point of metallic silver. The peak sintering time is measured in seconds[17,18]. During the sintering of the front-side solar silver paste, two main processes occur. Firstly, the silver particles undergo mutual sintering, forming conductive paths and densification[19,20]. Secondly, the glass powder softens, melts, and flows onto the silicon layer, establishing the interface connection between the silver electrode and the silicon solar cell[21–25]. The former process determines the resistivity of the silver electrode post-sintering, requiring close packing of silver particles and high sintering activity. The latter process influences the adhesion and contact resistance of the silver electrode post-sintering, requiring that the sintering densification of silver particles occurs later than the softening and flow of the glass powder. This prevents the reduction of pores after silver particle sintering, which could lead to glass residue in the silver layer. This not only increases the resistivity of the silver electrode but also results in insufficient glass interlayer at the silver-silicon interface[26–28]. Hence, it is generally considered that silver powder suitable for front-side solar silver paste should have an average particle size of 1-1.5 μm, a narrow size distribution, and high sphericity.

Current research on silver powder focuses on enhancing the sintering performance of silver paste through different shapes, particle sizes, and combinations of silver powders, the addition of submicron silver powders, and the construction of nanostructures[29–32]. These efforts aim to achieve denser silver electrodes and higher aspect ratios of silver grid lines[32–34]. Libin Mo et al[27]. investigated the effects of incorporating 0-10 wt% submicron spherical silver powder (average particle size of 0.3 μm) into micrometer-sized spherical silver powder (average particle size of 1 μm) on the rheological properties of silver paste, printed grid dimensions, sintering behavior, and cell electrical performance. The results indicated that the addition of submicron silver powder can improve the sintering performance of silver powder, reduce the porosity of the silver electrode surface, lower bulk resistivity, and increase the size of silver microcrystals precipitated on the silicon surface, thereby reducing contact resistivity. However, excessive addition of submicron silver powder can adversely affect the printability of silver paste, leading to a decrease in the aspect ratio of printed grid lines, an increase in series resistance, and a decrease in photoelectric conversion efficiency. Therefore, the addition of an appropriate amount of submicron silver powder needs to be considered holistically. Yongsheng Li et al[35]. developed microcrystalline spherical silver particles (SP-a) with internal pores. The study demonstrated that SP-a exhibits excellent sintering activity, forming a dense sintered body. At the Ag-Si interface, silver nanoparticles are formed, improving the silver-silicon contact. Photovoltaic cells constructed using SP-A exhibit low series resistance and high photoelectric conversion efficiency (19.26%).

The previous studies on silver powder performance have not addressed the influence of the compositional structure of silver powder particles on surface energy, sintering activity, and packing density. Silver powders prepared using the liquid-phase reduction method often exhibit similar external shapes and sizes, but their internal structures vary depending on the growth process. This paper focuses on investigating the impact of different growth processes on the microstructure of silver powder, analyzing its relationship with macroscopic physical properties and sintering performance of silver powder. Finally, it explores the influence of different silver powders on the sintering performance of silver paste and the electrical properties of solar cells.

 doi:10.20944/preprints202312.1871.v1

2. Materials and Methods

2.1. Materials

The silver powder used in this study was custom-made by Guiyan Platinum Co., Ltd., featuring various microstructures of micron-sized spherical silver powder. The glass powder employed was prepared using the melt-quenching method, with raw materials sourced externally without purification processing, comprising TeO_2 (≥99%, Aladdin Reagent Co. Ltd), Bi_2O_3 (≥99.0%, Aladdin Reagent Co. Ltd), B_2O_3 (≥98%, Aladdin Reagent Co. Ltd), ZnO (≥99%, Aladdin Reagent Co. Ltd), Al_2O_3 (≥99%, Aladdin Reagent Co. Ltd). The materials were proportionally weighed in a mass ratio of TeO_2 : Bi_2O_3 : B_2O_3 : ZnO : Al_2O_3 = 15 : 50 : 20 : 10 : 5, mixed thoroughly in an agate mortar, and melted at 1200°C for 30 minutes. The molten glass was quenched in deionized water at room temperature, and the obtained glass chunks were ball-milled and sieved to yield glass powder with an average particle size of 2.4 μm. The organic vehicle used consisted of a blend of ethyl cellulose (CP, Aladdin Reagent Co. Ltd), terpineol (≥95%, Aladdin Reagent Co. Ltd), butyl carbitol (≥99%, Shanghai Wokai Chemical Reagent Co., Ltd), butyl phthalate (≥99.5%, Sinopharm Chemical Reagent Co. Ltd), silane coupling agent KH-570 (≥98%, Sinopharm Chemical Reagent Co. Ltd), and hydrogenated castor oil (Aladdin Reagent Co. Ltd). The silver paste was formulated with a mass ratio of silver powder, glass powder and organic vehicle was 86 : 2 : 12, initially weighed and mixed, followed by further refinement through a three-roll mill to achieve a fineness of <5 μm.

2.2. Printing and metallization of Ag pastes

Various test patterns were printed on P-type monocrystalline silicon solar cells with a surface SiN_x antireflection coating (sheet resistance of 80 Ω/sq, size of 156×156 mm) using a screen-printing machine. For sheet resistance testing, 10 parallel lines, each 2 mm wide and 100 mm long, were printed. Adhesion testing involved printing square patterns of 20×20 mm, while performance testing of the solar cells utilized printed patterns consisting of 9 main grid lines and 104 Secondary grid lines with a width of 15 μm. Following printing, the solar cells were allowed to stand at room temperature for 10 minutes to allow the silver paste to level adequately. Subsequently, the cells were dried at 150 °C for 20 minutes and then subjected to metallization of the front silver paste through sintering in a continuous belt furnace. The peak sintering temperature was denoted as T_0, and the heating temperatures in different zones of the belt furnace were as follows: 300 °C / 300 °C / 300 °C / 500 °C / 590 °C / 600 °C / T_0-100 °C / T_0 / T_0-15 °C.

2.3. Measurement and Characterization

The microstructures of the silver powder, as well as the surface and cross-section of the silver electrode, were observed using field emission scanning electron microscopy (FESEM, Nova Nano SEM 450, FEI, USA). The particle size distribution of the silver powder was determined using image software (Image J). The number of measured silver particles exceeded or equaled 200. The specific surface area of the silver powders was analyzed using a surface area porosity analyzer (BET, BSD-PS1/2/4, BSD INSTRUMENT, China). The crystal structure of the silver powder was identified through X-ray diffraction (XRD, Empyrean, PANalytical B.V., Netherlands). Thermal properties were assessed using differential scanning calorimetry (DSC, Q2000, TA Corporation, USA) in air with a heating rate of 10 °C/min. The square resistance of the silver grids was measured with a multifunction digital four-probe tester (ST-2258C, Suzhou Lattice Electronics Co., Ltd, China). The aspect ratio of the silver grids was determined using a 3D digital microscope (Zeta-20, USA).

3. Results and discussion

3.1. microstructure and performance analysis of silver powder

3.1.1. microstructure of silver powder

Preprints (www.preprints.org) | NOT PEER-REVIEWED | Posted: 27 December 2023 doi:10.20944/preprints202312.1871.v1

Three types of micrometer-sized spherical silver powders (S1, S2, and S3) with distinct crystal structures were prepared by the liquid-phase reduction method through variations in reaction conditions. The microstructures and particle sizes of the silver powders were observed using field emission scanning electron microscopy (FESEM). As shown in Figure 1 (a1-c1), the surface of S1 silver powder is characterized by the aggregation of numerous silver crystallites, each in the size range of several tens of nanometers. Despite a non-smooth surface, S1 exhibits high sphericity with no sharp edges. For S2 silver powder, as depicted in Figure 1 (a2-c2), larger silver crystallites aggregate on the surface, resulting in higher roughness and an almost spherical appearance with a few angular features. In the case of S3 silver powder, the surface is predominantly formed through crystal growth, presenting a smooth yet polyhedral appearance with edges. The average particle sizes for S1, S2, and S3 are approximately 1.23 μm, 1.26 μm, and 1.04 μm, respectively. S1 and S3 exhibit a higher concentration in particle size distribution, with S1 displaying a distribution closest to a normal distribution. Conversely, the particle size distribution for S2 is less concentrated, with a more uniform distribution across different particle sizes.

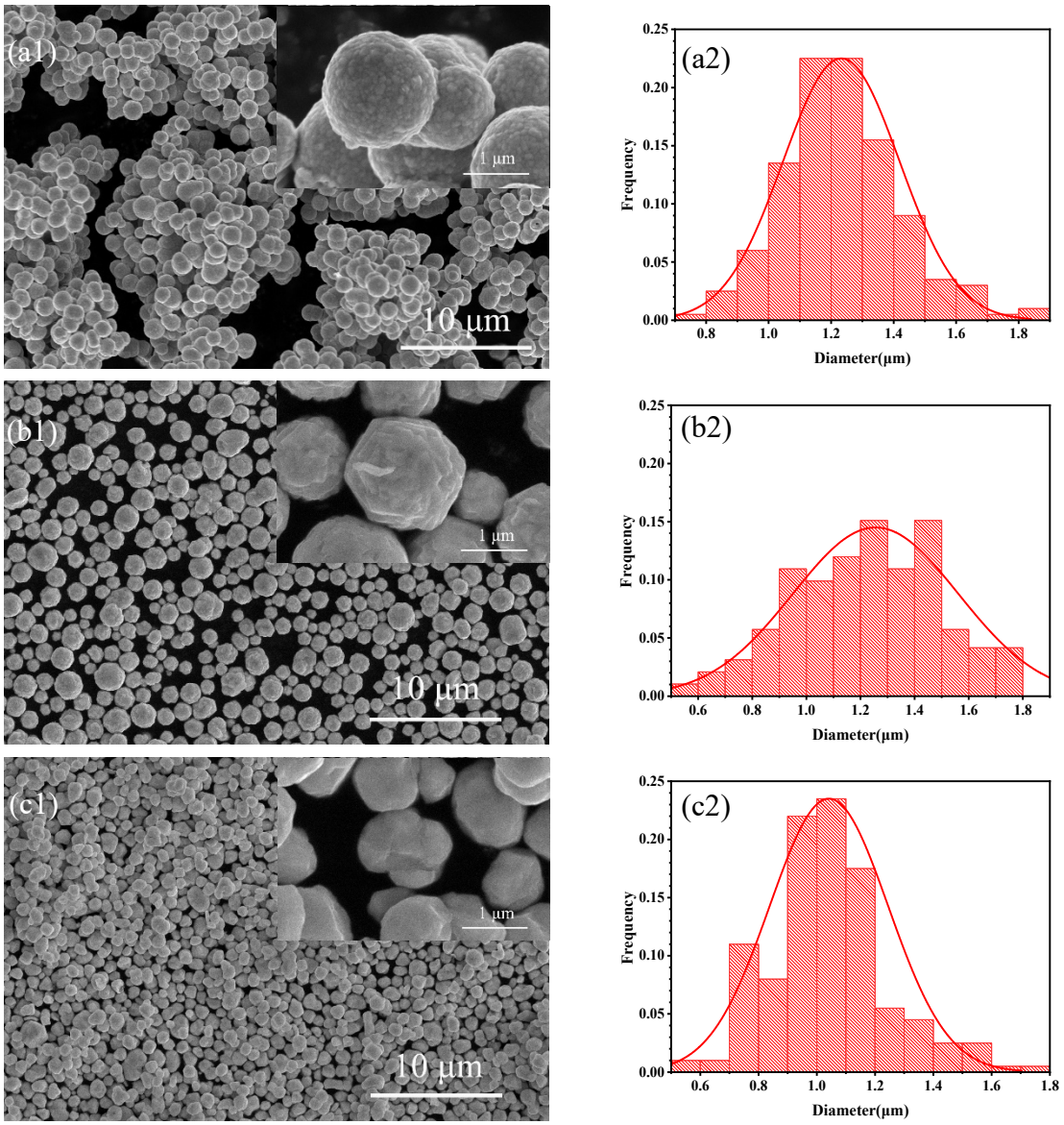

Figure 1. SEM images of different silver powders (a1) S1, (b1) S2, (c1) S3; Particle size distributions of different silver powders (a2) S1, (b2) S2, (c2) S3.

The X-ray diffraction (XRD) patterns of silver powders S1 to S3 were examined, and the results are presented in Figure 2. It is evident that the diffraction peaks for all three silver powders

Preprints (www.preprints.org) | NOT PEER-REVIEWED | Posted: 27 December 2023 doi:10.20944/preprints202312.1871.v1

correspond precisely to the standard PDF card for silver (PDF#87-0597), without any impurity peaks, indicating the purity of the silver in each powder. Additionally, an analysis of the three main crystallographic planes' peak intensities and full-width at half-maximum (FWHM) values for silver powders S1 to S3, as summarized in Table 1, reveals notable changes in the strongest (111) crystallographic plane of S1, the peak intensity decreases, and the FWHM increases, indicative of broadening diffraction peaks. Typically, peak broadening occurs when the crystallite size is below 100 nm or when there are microstrains present in the sample. Since silver powders prepared via the liquid-phase reduction method generally do not undergo mechanical processing, microstrains are unlikely. This observation, coupled with the SEM magnified image in Figure 1 (a1), suggests that silver powder S1 is composed of aggregated small grains, each smaller than 100 nm.

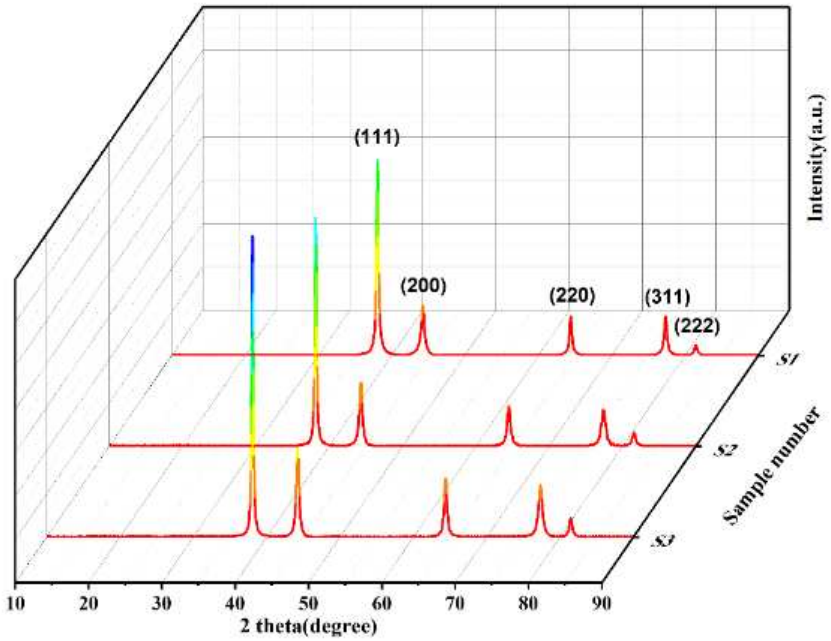

Figure 2. XRD diffraction patterns of different spherical silver powders.

Table 1. Diffraction peak intensity and FWHM of different crystal planes of silver powder.

Sample	(111) facet		(200) facet		(220) facet	
	Intensity	FWHM	Intensity	FWHM	Intensity	FWHM
S1	2203	0.343	535	0.505	427	0.412
S2	2608	0.300	709	0.480	448	0.506
S3	3454	0.298	998	0.450	654	0.452

3.1.2. analysis of the growth process of silver powder

The liquid-phase reduction method for silver powder involves two main steps: nucleation and growth. According to classical nucleation theory, crystalline nuclei begin to form in a solution when the solution's supersaturation surpasses a critical threshold that overcomes the nucleation barrier[36]. Once nuclei are formed, the powder enters a growth stage, which occurs through two mechanisms. In one mechanism, small nanocrystalline nuclei in the solution aggregate directly, and due to the high surface energy at contact points between particles, silver grows by bonding the particles together. This aggregation-bonding process repeats, leading to the continuous growth and aggregation of silver powder particles. The other mechanism involves direct growth along crystal faces. Given silver's face-centered cubic crystal structure, Fm3m space group symmetry, and minimal variation in surface energies across different crystal faces, silver particles tend to grow into quasi-spherical polyhedra without growth orientation intervention. The schematic diagram of the silver powder

Preprints (www.preprints.org) | NOT PEER-REVIEWED | Posted: 27 December 2023 doi:10.20944/preprints202312.1871.v1

growth process is illustrated in Figure 3. Silver powder S1 represents a typical polycrystalline aggregation type, S3 reflects crystal-growth-type silver powder, and S2 is a hybrid type where both crystal growth and aggregation occur. In the preparation of silver powder, when the rate of crystal aggregation exceeds the rate of crystal growth, particularly in highly supersaturated reaction solutions leading to explosive nucleation in the early stages, the predominant mechanism is particle aggregation, resulting in silver powder resembling S1. Conversely, when the reaction solution has a lower supersaturation level, and the addition of the solution is prolonged, limiting the initial nucleation or the aggregation process with the use of protective agents, crystal growth becomes the dominant mechanism, yielding silver powder similar to S3. It is noteworthy that excessive protective agent content or exceptionally low solution supersaturation can lead to preferential crystal growth, resulting in non-spherical particles such as flakes, rods, or branched structures.

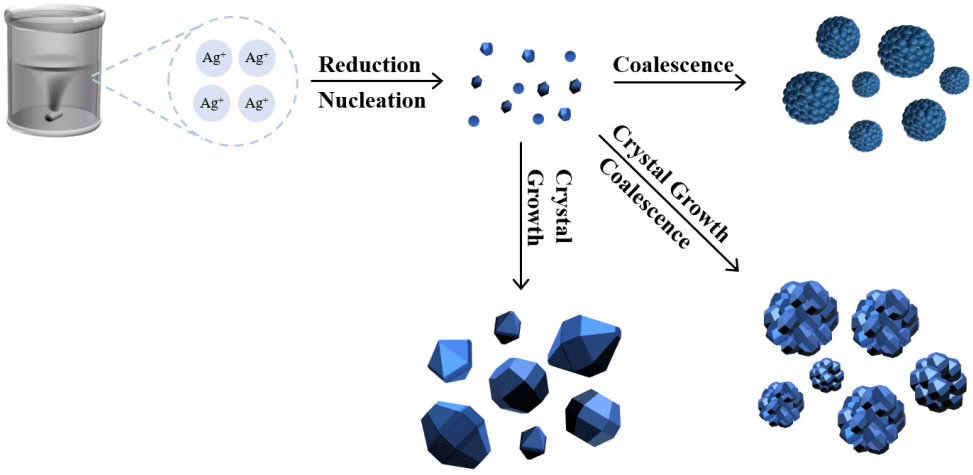

Figure 3. Schematic diagram of silver powder growth process.

3.1.3. analysis of macroscopic physical properties of silver powder

The macroscopic physical properties of silver powders S1-S3 are presented in Table 2. Tap density and specific surface area are two crucial performance parameters for solar silver pastes. Higher tap density indicates the silver powder's ability to form denser packing, resulting in a more compact silver layer during paste sintering. Smaller specific surface area suggests a reduced surface area requiring wetting, leading to lower organic vehicle content in rolled pastes with similar flow characteristics and fewer voids left after the organic vehicle volatilizes during sintering. Generally, for micrometer-sized silver powders with similar surface conditions, larger average particle size corresponds to higher tap density and smaller specific surface area. Although the average particle sizes of silver powders S1 and S2 are close and both larger than that of silver powder S3, the measured tap density follows the order S3 > S2 > S1, while the specific surface area follows S3 < S2 < S1. This observation is speculated to be due to the presence of surface grains of different sizes on silver powders S1 and S2, contributing to increased specific surface area. Silver powder S2, with some smooth surfaces, exhibits a smaller specific surface area than S1. Additionally, the existence of surface grains implies more grain boundaries on the surfaces of S1 and S2, indicating higher surface energy. Elevated surface energy tends to promote particle aggregation, resulting in larger interparticle gaps and reduced compaction during packing, leading to lower tapped density. Similar-shaped and sized silver powders exhibit significant macroscopic differences in performance. Therefore, in selecting silver powders, it is imperative to consider not only their shape and size but also their microstructure.

Preprints (www.preprints.org) | NOT PEER-REVIEWED | Posted: 27 December 2023 doi:10.20944/preprints202312.1871.v1

Table 2. Macroscopic physical properties of silver powder S1-S3.

Sample	Average particle size (μm)	Tap density (g/cm³)	Specific surface area (m²/g)	Ignition loss (%)
S1	1.23	3.34	0.92	0.87
S2	1.26	4.67	0.67	0.63
S3	1.06	5.52	0.41	0.35

3.1.4. Thermal performance analysis of silver powder

The DSC test results for silver powders S1-S3 are illustrated in Figure 4. Silver powder S1 exhibits a distinct exothermic peak around 300 °C, presumed to be associated with the decomposition of Ag_2O on the silver powder surface. The corresponding reaction is represented by Equation (1), indicating Ag_2O decomposition, which generally occurs in the range of 250-300 °C, constituting an exothermic process. Unlike many metals that tend to oxidize at high temperatures, silver undergoes oxidation at lower temperatures. At elevated temperatures, Ag_2O decomposes, reverting to elemental silver. Both silver powders S2 and S3 show a small exothermic peak around 250 °C, with S2's peak being less pronounced. Table 1 indicates that silver powder S1 exhibits the highest mass loss during decomposition, likely attributed to its elevated surface energy. The abundance of Ag_2O on the surface of silver powder S1 at room temperature may contribute to the significant exothermic peak and substantial mass loss observed at 300 °C. The pre-melting sintering reaction of silver powder is another exothermic process influenced significantly by the surface energy of the powder. In Figure 4, the DSC curve for silver powder S1 exhibits an increased slope around 450 °C, suggesting the initiation of sintering. Similarly, the sintering onset temperature for silver powder S2 is observed at approximately 500 °C, while that for silver powder S3 falls within the range of 550-600 °C.

$$2Ag_2O \rightarrow 2Ag+O_2\uparrow \quad (1)$$

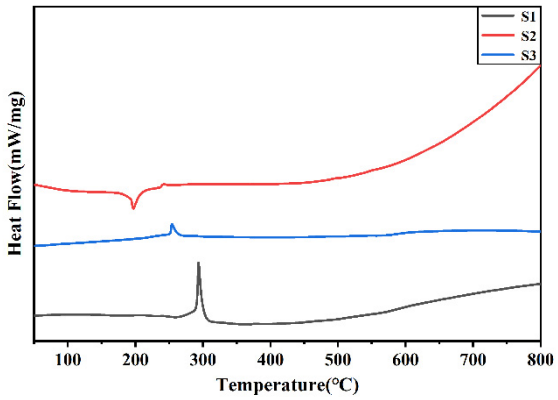

Figure 4. DSC curve of silver powder S1-S3.

3.2. Effect of different silver powders on sintering properties of silver slurry

3.2.1. Analysis of square resistance and adhesion of silver paste after sintering

Silver pastes, denoted as SP1-SP3, were prepared using silver powders S1-S3, and subjected to sintering at various peak temperatures to investigate the impact of silver powder sintering properties on the sheet resistance and adhesion strength of the resulting silver electrodes. The measured results for sheet resistance and adhesion strength are presented in Figure 5. It is evident that at lower sintering temperatures, SP1 exhibits lower sheet resistance and higher adhesion strength, indicating favorable sintering activity for SP1 silver powder at lower temperatures, consistent with the DSC test results. As the sintering temperature gradually increases, the sheet resistance of SP2 and SP3 rapidly decreases, accompanied by a rapid increase in adhesion strength. When sintering temperature

 doi:10.20944/preprints202312.1871.v1

reaches 810 °C, the sheet resistance of SP3 is comparable to that of SP1, and at 840 °C, the sheet resistance of SP3 is lower than that of SP1. The sheet resistance of SP2 consistently remains higher than that of SP1, and beyond 840 °C, the sheet resistance of SP1 and SP3 becomes similar. At 780 °C, the adhesion strength of SP3 surpasses that of SP1, and at 810 °C, the adhesion strength of SP2 exceeds that of SP1. After sintering at 810 °C, the variation in adhesion strength among the three silver pastes becomes minor, with a noticeable decline only at 900 °C. Considering the sheet resistance and adhesion strength of the three silver pastes at different sintering temperatures, it is evident that the sintering performance of SP1 surpasses that of SP2 and SP3 when the sintering temperature is below 810 °C. However, when the sintering temperature exceeds 810 °C, the sintering performance of SP3 becomes superior to that of SP1 and SP2.

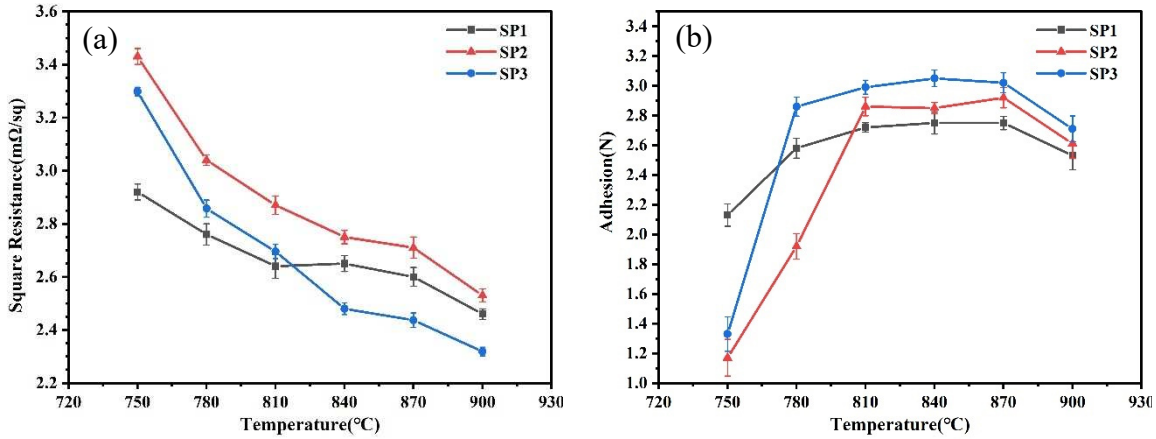

Figure 5. Properties of three silver pastes sintered at different peak temperatures, (a) square resistance, (b) adhesion.

3.2.2. Surface and section micro morphology of silver paste after sintering

Due to the suboptimal sintering performance of silver paste SP2 at both low and high-temperature ranges, distinctive silver pastes SP1 and SP3 were selected for observation via SEM, focusing on their surface and cross-sectional microstructures after sintering at 750 °C, 840 °C, and 900 °C, as depicted in Figures 6 and 7, respectively. Comparing Figures 6(a) and 6(d), at 750 °C sintering, the necking between silver powder S1 particles has largely disappeared, indicating a trend toward mutual fusion and the formation of a conductive network, resulting in lower sheet resistance. In contrast, silver powder S3 exhibits partially formed necks between particles, with some particles just making contact without starting the sintering process, leading to a higher sheet resistance. Observing Figure 6(b) and 6(e) at 840 °C sintering, both silver powders S1 and S3 have entered the sintering shrinkage stage, with silver particles starting to fuse and grow. Due to the higher tap density of silver powder S3, resulting in a denser initial packing, the sintered layer of S3 demonstrates superior density and lower sheet resistance. Examining Figure 6(c) and 6(f) at 900 °C sintering, a melting tendency is observed in the silver powders, with crystal growth steps rapidly forming on the particle surfaces. The initial packing density of the silver powder begins to dominate over the sintering activity, leading to a modest decrease in sheet resistance for all three silver pastes, with SP3 exhibiting the lowest sheet resistance.

Preprints (www.preprints.org) | NOT PEER-REVIEWED | Posted: 27 December 2023 doi:10.20944/preprints202312.1871.v1

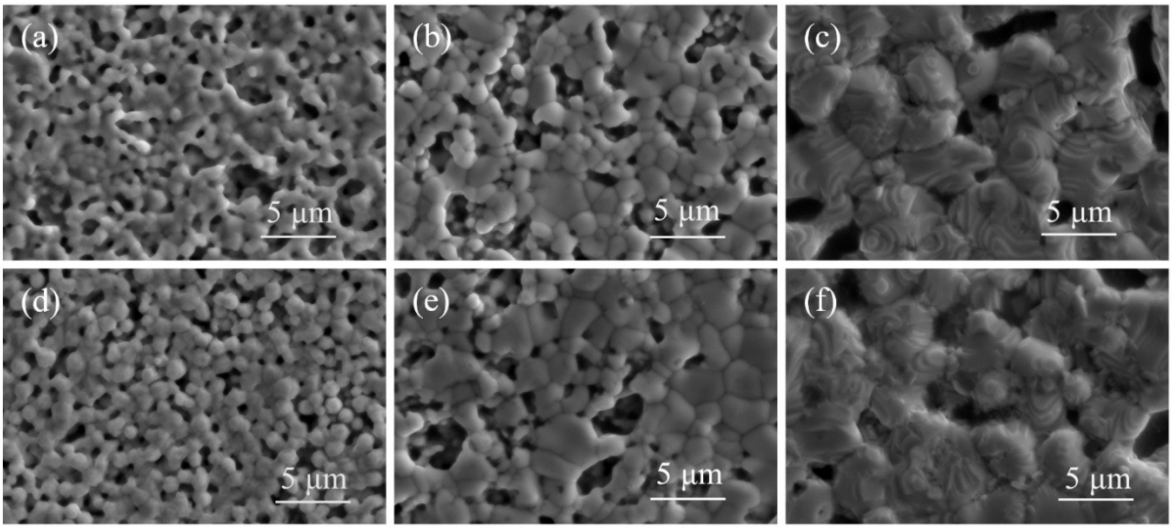

Figure 6. SEM images of silver paste Sp1 and SP3 sintered at different peak temperatures, (a) 750 ℃, SP1; (b) 840 ℃, SP1; (c) 900 ℃, SP1; (d) 750 ℃, SP3; (e) 840 ℃, SP3; (f) 900 ℃, SP3.

Comparing Figure 7(a) and 7(d), at 750 °C sintering, the cross-sectional observation of the silver powder aligns with the surface findings. In the case of silver powder S3, the particles are not fully interconnected, resulting in fractures within the silver layer upon detachment, indicating poor adhesion for silver paste SP3. Contrasting Figure 7(b) and 7(e) at 840 °C sintering, the silver powder has achieved relatively dense sintering, with channels between particles for glass powder flow closed. Some glass melt remains trapped within the silver layer, particularly noticeable in silver paste SP1 due to its higher sintering activity, resulting in a thicker glass layer between the silver layer and silicon. Consequently, SP1 exhibits higher sheet resistance and lower adhesion compared to SP3. Examining Figure 7(c) and 7(f) at 900 °C sintering, the closure of channels in the silver powder accelerates, increasing the glass content within the silver layer and reducing the glass layer between the silver layer and silicon. This leads to a decrease in adhesion for all three silver pastes. Additionally, at higher temperatures, the reaction between glass and SiN_x anti-reflective layer becomes more intense, generating gas due to the reaction. As the channels within the silver layer close prematurely, some gas remains trapped within the glass layer, forming voids, as outlined by the red dashed circles in the diagram. This phenomenon further contributes to the reduction in adhesion, potentially leading to delamination beneath the silver layer.

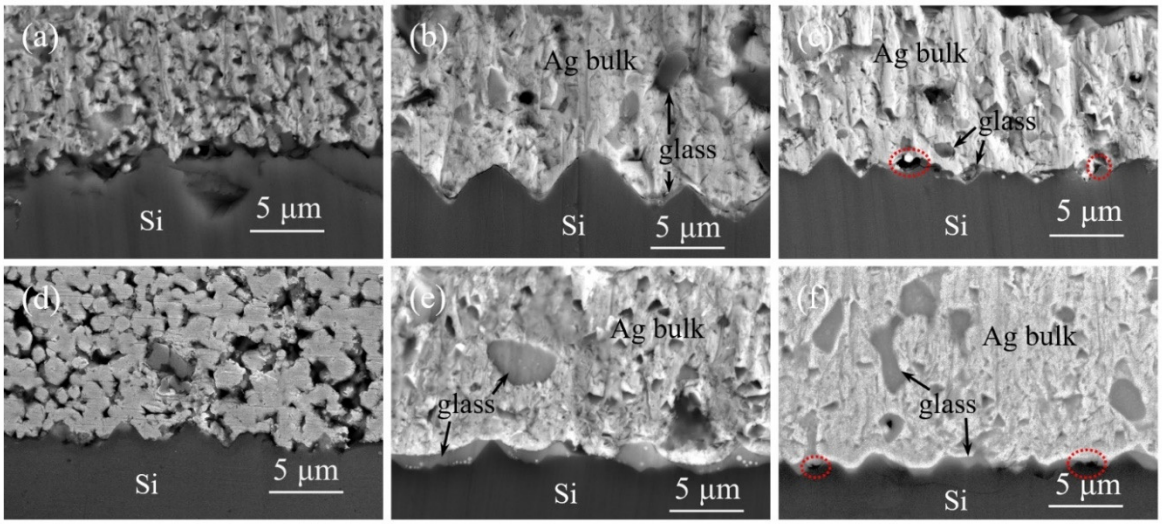

 doi:10.20944/preprints202312.1871.v1

Figure 7. SEM cross sections of silver paste Sp1 and SP3 sintered at different peak temperatures, (a) 750 ℃, SP1; (b) 840 ℃, SP1; (c) 900 ℃, SP1; (d) 750 ℃, SP3; (e) 840 ℃, SP3; (f) 900 ℃, SP3.

3.3. Effects of different silver powders on the morphology and electrical properties of solar cells

Silver pastes, SP1-SP3, were printed onto solar cells using a mesh screen with a fine grid width of 15 μm. After sintering at 840 °C, the morphology of the grid lines was examined using a 3D digital microscope, and the aspect ratio was measured, as depicted in Figure 8 and summarized in Table 3. Figure 8 reveals distinct segments in the silver grid lines of SP1, whereas those of SP2 and SP3 appear more uniformly flat. The cross-sectional overlap images in (a2) - (c2) indicate good alignment of the contour lines for SP2 and SP3. Although SP1 exhibits significant variations in peak heights, even the smallest contour lines cover a sufficient area for effective electrical conduction, preventing grid line breaks. Given that silver powders S1-S3 undergo the same surface treatment process and exhibit similar shapes and particle sizes when processed into silver pastes (SP1-SP3), their printing characteristics are comparable. However, due to differences in the compactness of particle stacking after drying, SP1 displays the lowest stacking density. Additionally, owing to the high surface energy and sintering activity of silver powder S1, SP1 experiences the most pronounced sintering shrinkage, resulting in substantial axial contraction stress in the grid lines. Beyond a certain limit, this stress leads to segmented contraction of the grid lines.

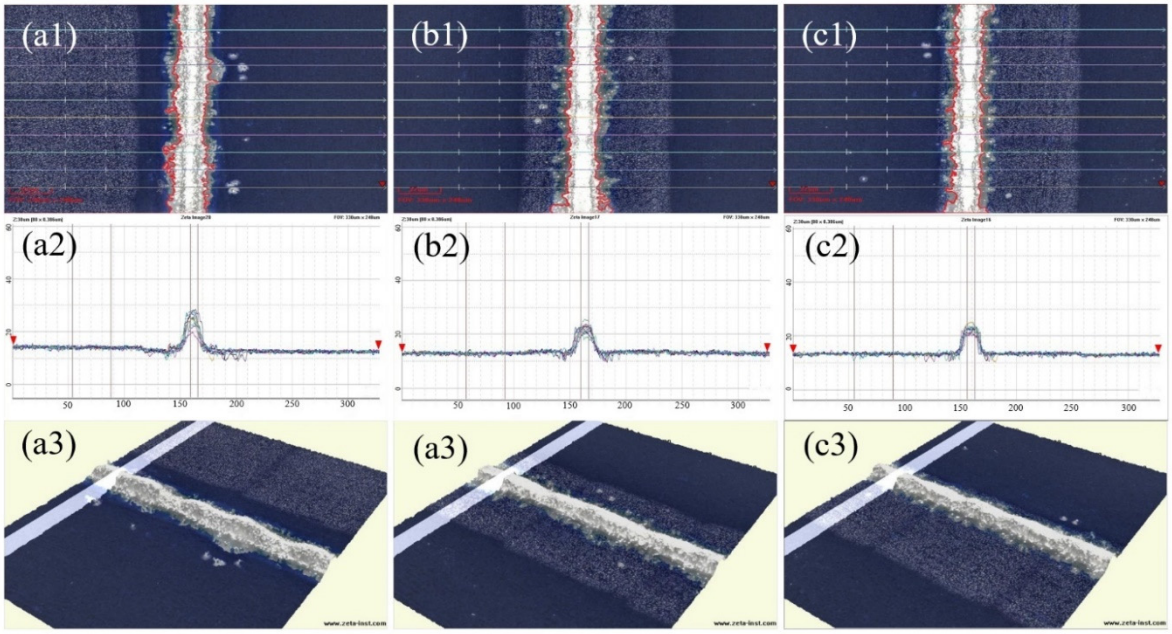

Figure 8. 3D microscopic surface images of silver grids of solar cells used different silver pastes, (a1) SP1; (b1) SP2; (c1) SP3. Overlap image of cross section of silver grids of solar cells used different silver pastes, (a2) SP1; (b2) SP2; (c2) SP3. 3D images of silver grids of solar cells used different silver pastes, (a3) SP1; (b3) SP2; (c3) SP3.

Table 3 reveals that the aspect ratios of silver grid lines in SP1-SP3 are comparable and generally high. This characteristic is advantageous for minimizing both the shading area and electrical resistance of the silver grid lines. Consequently, it contributes to the reduction of series resistance in solar cells, thereby enhancing the photoelectric conversion efficiency. Notably, SP3 exhibits the highest aspect ratio among the sintered silver pastes, while SP2 demonstrates the most uniform size distribution of silver grid lines. The narrowest width of the sintered grid lines among the three pastes is 4.49 μm, with a corresponding height of 17.8 μm, confirming their satisfactory conductivity.

Preprints (www.preprints.org) | NOT PEER-REVIEWED | Posted: 27 December 2023 doi:10.20944/preprints202312.1871.v1

Table 3. The height, width and aspect ratio of silver grids of solar cells used different silver pastes.

cross section	SP1			SP2			SP3		
	Height (μm)	Width (μm)	H/W Ratio	Height (μm)	Width (μm)	H/W Ratio	Height (μm)	Width (μm)	H/W Ratio
1	10.07	27.86	0.36	9.68	25.80	0.38	7.89	22.20	0.36
2	12.23	40.51	0.30	8.02	23.20	0.35	9.88	22.20	0.45
3	12.80	36.40	0.35	6.00	23.74	0.25	9.21	25.54	0.36
4	4.49	17.80	0.25	10.37	23.48	0.44	6.90	25.00	0.28
5	10.30	22.40	0.46	7.99	24.51	0.33	11.45	23.20	0.49
6	10.10	25.54	0.40	11.82	26.60	0.44	7.44	29.93	0.25
7	10.94	33.80	0.32	9.57	26.32	0.36	9.69	18.10	0.54
8	13.54	29.20	0.46	7.48	21.16	0.35	9.06	22.40	0.40
9	7.21	19.90	0.36	8.68	21.93	0.40	7.59	20.60	0.37
10	8.66	22.70	0.38	8.37	23.20	0.36	10.03	21.16	0.47
Min	4.49	17.80	0.25	6.00	21.16	0.25	6.90	18.10	0.25
Max	13.54	40.51	0.46	11.82	26.60	0.44	11.45	29.93	0.54
Mean	10.03	27.61	0.37	8.80	24.00	0.37	8.92	23.04	0.40

The I-V performance tests were conducted on the solar cells printed with silver pastes SP1-SP3, and the results are presented in Table 4. It is evident that the three silver pastes exhibit minimal influence on the parallel resistance (R_{sh}) and open-circuit voltage (V_{oc}) of the solar cells. SP1 shows the lowest series resistance (R_s) and the highest short-circuit current (I_{sc}). This outcome may be attributed to the high surface energy of silver powder S1, leading to a higher proportion of silver entering the glass melt during sintering. Consequently, a large number of silver nanocrystals precipitate in the glass layer between the silver layer and silicon, resulting in low contact resistance, lower Rs, and higher Isc in the solar cells. SP3 demonstrates the highest fill factor (FF), possibly due to its silver grid lines having the maximum aspect ratio, minimizing shading and, thus, increasing FF. In terms of overall photoelectric conversion efficiency, both SP1 and SP3 are comparable and outperform SP2.

Table 4. I-V performance test results of solar cells used different silver pastes.

Paste	I_{sc} (A)	V_{oc} (V)	R_s (mΩ)	R_{sh} (Ω)	FF (%)	Eta (%)
SP1	13.67	0.6869	1.23	847	81.37	23.15
SP2	13.62	0.6872	1.57	848	81.42	23.09
SP3	13.64	0.6870	1.43	853	81.59	23.17

4. Conclusions

In situations where the shape and size of silver powders are similar, the compositional structure significantly influences their performance. Polycrystalline aggregative silver powders, formed through the aggregation of fine microcrystals, exhibit higher surface energy, resulting in easy particle agglomeration and relatively low packing density. This condition has a certain impact on the sintering density of silver pastes. However, the high sintering activity of these silver powders ensures favorable sintering performance for the silver paste at temperatures below 800°C. When paired with glass frits with lower melting temperatures and better melt fluidity, the sintering window temperature of the silver paste can be effectively reduced. In contrast, crystalline silver powders primarily formed through crystal growth exhibit smooth surfaces, lower surface energy, high packing density, and easy wetting by organic carriers, facilitating the preparation of silver pastes with higher solid content. Crystalline silver powders also demonstrate excellent sintering activity at

high temperatures, coupled with high particle packing density and minimal sintering shrinkage, making them suitable for finer grid line printing processes.

Author Contributions: Conceptualization, Xianglei Yu, Junpeng Li and Guoyou Gan; Data curation, Xianglei Yu, Hu Sun, Zuo Qian and Wei Li; Formal analysis, Xianglei Yu; Funding acquisition, Junpeng Li and Guoyou Gan; Investigation, Xianglei Yu and Fuchun Huang; Methodology, Xianglei Yu and Hu Sun; Project administration, Guoyou Gan; Resources, Junpeng Li and Guoyou Gan; Software, Zuo Qian; Supervision, Weichao Li and Fuchun Huang; Validation, Xianglei Yu, Hu Sun, Weichao Li and Wei Li; Visualization, Xianglei Yu and Zuo Qian; Writing – original draft, Xianglei Yu; Writing – review & editing, Xianglei Yu, Junpeng Li and Guoyou Gan. All authors have read and agreed to the published version of the manuscript.

Funding: Please add: This research was funded by National Natural Science Foundation of China, Grant number 51771084; the Major Science and Technology project of Yunnan Province, Grant number 202102AB080008; the Science and Technology projects of Yunnan Precious Metals Laboratory, Grant number YPML-2022050207 and YPML-2023050206; Joint project of enterprise basic research and application basic research in Yunnan Province, Grant number 202101BC070001-017.

Data Availability Statement: The data that support the findings of this study are available from the corresponding author, upon reasonable request.

Conflicts of Interest: The authors declare no conflict of interest.

References

1. Sun, X. J.; Xing, J. J.; Yang, Y. X.; Yuan, X.; Li, H. B.; Tong, H., Ohimc Contact Formation Mechanism of Silver-Aluminum Paste Metallization on the p+ Emitter of n-Type Crystalline Silicon Solar Cells. *Journal of Electronic Materials* **2022,** 51, (10), 5717-5722.
2. Li, Q.; Ma, S.; Wang, H.; Bai, J.; Bi, S.; Wang, H., Effect of rare metal oxide doped lead-based glass frits on the performance of crystalline silicon solar cells. *Solar Energy Materials and Solar Cells* **2023,** 254.
3. Xie, X.; Xu, Y.; Chen, F., Effect of PbO content in glass on front silver paste ohmic contact performance of solar cell. *Journal of Functional Materials* **2022,** 53, (5).
4. Deng, D.; Chen, Z.; Hu, Y.; Tong, Y.; Liang, X., Preparation and post-treatment of silver powders for front contact pastes of silicon solar cells. *International Journal of Materials Research* **2021**.
5. Fu, M.; Li, H. Y.; Wang, Y.; Fan, L.; Chen, D.; Feng, Z., Study on the Synthesis and Performances of Ultrafine Silver Powder Used as Silicon Solar Cell Front Silver Contacts. *Materials Science Forum* **2016,** 852, (pt.1), 378-384.
6. Wang, G.; Wang, H.; Cui, Y.; Bai, J., Preparation of micro-sized and monodisperse crystalline silver particles used for silicon solar cell electronic paste. *Journal of Materials Science: Materials in Electronics* **2013,** 25, (1), 487-494.
7. Qin, J.; Zhang, W. J.; Yang, J. C.; Du, G. B.; Cai, X., Tailor the Rheological Properties of Silver Front Side Metallization Paste for Crystalline Silicon Solar Cells. *Materials Science Forum* **2019,** 956, 12-20.
8. Aal, K. A.; Willenbacher, N., Front side metallization of silicon solar cells - A high-speed video imaging analysis of the screen printing process. *Solar Energy Materials and Solar Cells* **2020,** 217, 8.
9. Mo, L. B.; Zhao, L.; Zhou, C. L.; Zhang, Y. Y.; Wang, W. J., Application of Ethyl Cellulose and Polyamide Wax in Silicon Solar Cell Electrodes. *Rare Metal Mat. Eng.* **2019,** 48, (3), 994-1000.
10. Sun, Y.; Xue, H.; Yang, C.; Tian, Y.; Ning, S.; Ma, S.; Wang, H., Improvement of wettability of Te-modified lead-free glass frit and its effect to front side silver paste in crystalline silicon solar cells. *Solar Energy Materials and Solar Cells* **2023,** 253.
11. Mo, L.; Zhao, L.; Zhou, C.; Wang, G.; Wang, W., Effect of TeO2 on Ag/Si interface contact of crystalline silicon solar cells. *Materials Letters* **2022,** 324.
12. Kim, Y.; Nakayama, T.; Kim, H., Effect of Te-based glass on contact formation and electrical properties in Si solar cells. *Journal of Alloys and Compounds* **2020,** 829.
13. Feng, B.; Liu, Y.; Chen, W.; Xing, G.; Chen, X.; Du, X., Differently shaped Ag crystallites and four current transport paths at sintered Ag/Si interface of crystalline silicon solar cells. *Solar Energy Materials and Solar Cells* **2023,** 257.
14. Zhang, J.; Zhou, J.; Huang, J.; Lv, B., Effect of TeO2-based lead-free glass on contact formation of front side silver metallization for monocrystalline silicon solar cells. *Solar Energy Materials and Solar Cells* **2022,** 238.
15. Lan, F.; Bai, J.; Wang, H., The preparation of oleylamine modified micro-size sphere silver particles and its application in crystalline silicon solar cells. *RSC Advances* **2018,** 8, (30), 16866-16872.
16. Wang, H.; Tai, Y.; Li, R.; Wang, H.; Bai, J., Effect of the mass ratio of micron and submicron silver powder in the front electrode paste on the electrical performance of crystalline silicon solar cells. *RSC Advances* **2016,** 6, (34), 28289-28297.

17. Yang, W. C.; Sun, Q.; Lei, Q.; Zhu, W. B.; Li, Y. F.; Wei, J.; Li, M. Y., Formation of a highly conductive thick film by low-temperature sintering of silver paste containing a Bi2O3-B2O3-ZnO glass frit. *J. Mater. Process. Technol.* **2019,** 267, 61-67.
18. Schmidt, J.; Peibst, R.; Brendel, R., Surface passivation of crystalline silicon solar cells: Present and future. *Sol. Energy Mater. Sol. Cells* **2018,** 187, 39-54.
19. Kumar, P.; Aabdin, Z.; Pfeffer, M.; Eibl, O., High-efficiency, single-crystalline, p- and n-type Si solar cells: Microstructure and chemical analysis of the glass layer. *Sol. Energy Mater. Sol. Cells* **2018,** 178, 52-64.
20. Li, W.; Yu, C. X.; Wang, Y. K.; Yao, Y.; Yu, X. L.; Zuo, C.; Yu, Y., Experimental Investigation of Effect of Flake Silver Powder Content on Sintering Structure and Properties of Front Silver Paste of Silicon Solar Cell. *Materials* **2022,** 15, (20), 14.
21. Pi, X. X.; Cao, X. H.; Chen, J. S.; Zhang, L.; Fu, Z. X.; Wang, L. X.; Zhang, Q. T., Improved Ag-Si interface performance for Si solar cells using a novel Te-based glass and recrystallization process of Ag. *Rare Metals* **2021,** 40, (1), 84-89.
22. Sun, X.; Yao, S.; Xing, J.; Zhang, J.; Yang, Y.; Li, H.; Tong, H.; Yuan, X., Mechanism of silver/glass interaction in the metallization of crystalline silicon solar cells. *Materials Research Express* **2020,** 7, (1).
23. Li, H.; Tong, H.; Zhang, J.; Li, G.; Yang, Y.; Liu, C.; Li, H.; Yuan, X., Investigation on PbO–B2O3–SiO2–RxOy Glasses Applied in Noncontact Silver Paste for Crystalline Silicon Solar Cells. *Journal of Electronic Materials* **2020,** 49, (9), 5422-5429.
24. Gao, Z.; Jiang, X.; Wang, X. B.; Chen, Y. J.; Liu, J.; Chen, H. B.; Lin, Y.; Pan, F., Rare-earth element doping in glass frit for improved performance in silicon solar cells. *Funct. Mater. Lett.* **2019,** 12, (6), 4.
25. Chen, X. Y.; Xue, W. J.; Qin, Y.; Jiang, X. L.; Yin, H. P.; Shan, W., Effect of Al2O3 film on silver paste contact formation at silicon surface. *Solar Energy* **2017,** 158, 917-921.
26. Lan, S.-H.; Lee, C.-T.; Lai, Y.-S.; Chen, C.-C.; Yang, H.-W., The Relationship between the Structure and Thermal Properties of Bi2O3-ZnO-B2O3 Glass System. *Advances in Condensed Matter Physics* **2021,** 2021, 2321558.
27. Mo, L.; Zhang, Y.; Zhao, L.; Zhou, C.; Wang, W., Effect of sub-micrometer sized silver particle on the performance of the front Ag paste for c-Si solar cells. *Journal of Alloys and Compounds* **2018,** 742, 256-262.
28. Glatthaar, R.; Schmidt, F. P.; Hammud, A.; Lunkenbein, T.; Okker, T.; Huster, F.; Seren, S.; Greven, B. C.; Hahn, G.; Terheiden, B., Silver Metallization with Controlled Etch Stop Using SiO_x Layers in Passivating Contacts for Improved Silicon Solar Cell Performance. *Sol. RRL* **2023,** 7, (21), 9.
29. Tepner, S.; Wengenmeyr, N.; Linse, M.; Lorenz, A.; Pospischil, M.; Clement, F., The Link between Ag-Paste Rheology and Screen-Printed Solar Cell Metallization. *Adv. Mater. Technol.* **2020,** 5, (10), 9.
30. Oh, W.; Park, J.; Dimitrijev, S.; Kim, E. K.; Park, Y. S.; Lee, J., Metallization of crystalline silicon solar cells for shingled photovoltaic module application. *Solar Energy* **2020,** 195, 527-535.
31. Rudolph, M.; Kruse, C.; Wolter, H.; Wolpensinger, B.; Baumann, U.; Bräunig, S.; Ripke, M.; Falcon, T.; Brendel, R.; Dullweber, T. In *PERC plus Solar Cells with Screen-Printed Dashed Ag Front Contacts*, 9th International Conference on Crystalline Silicon Photovoltaics (SiliconPV), Imec, Leuven, BELGIUM, Apr 08-11, 2019; Amer Inst Physics: Imec, Leuven, BELGIUM, 2019.
32. Musztyfaga-Staszuk, M.; Janicki, D.; Panek, P., Correlation of Different Electrical Parameters of Solar Cells with Silver Front Electrodes. *Materials* **2019,** 12, (3), 366.
33. Zhang, J. F.; Yuan, X.; Tong, H.; Yang, Y. X.; Zhao, H.; Li, H. B., Effect of glass phase and temperature on contact resistance between Ag and Al electrodes. *Materials Research Express* **2019,** 6, (3), 8.
34. Jonai, S.; Tanaka, A.; Muramatsu, K.; Saito, G.; Nakamura, K.; Ogura, A.; Ohshita, Y.; Masuda, A., Effect of additives in electrode paste of p-type crystalline Si solar cells on potential-induced degradation. *Solar Energy* **2019,** 188, 1292-1297.
35. Li, Y.; Chen, Z.; Zhou, R.; Zhao, W.; Huang, Z.; Liu, J.; Yang, M.; Pan, F., Design of advanced porous silver powder with high-sintering activity to improve silicon solar cells. *Nano Res.* **2023**, 9.
36. Tang, X. J.; Gan, G. Y.; Yu, X. L.; Li, J. P., A Method for Preparing AgNWs with Accelerated Seed-Wire Conversion Time. *Metals* **2023,** 13, (4), 10.